Nanoscale

PAPER

View Article Online
View Journal | View Issue

Cite this: *Nanoscale*, 2024, **16**, 14757

Tailoring sensitization properties and improving near-infrared photon upconversion performance through alloying in superatomic molecular Au_{25} nanoclusters†

Masaaki Mitsui, * Yuki Miyoshi and Daichi Arima

Noble-metal nanoclusters (NCs) protected by organic ligands have recently come to the forefront as potent triplet sensitizers for photon upconversion (UC) *via* triplet–triplet annihilation (TTA), owing to their capacity for atomic-level photophysical property customization. Among these, the rod-shaped bi-icosahedral $[Au_{25}(PPh_3)_{10}(S\text{-}C_2H_4Ph)_5Cl_2]^{2+}$ (**Au-rod**) NC is a particularly iconic superatomic molecular NC, recently identified as a near-infrared (NIR)-absorbing sensitizer for TTA-UC. In this study, we synthesized Cu-doped NCs, $[Au_{25-x}Cu_x(PPh_3)_{10}(S\text{-}C_2H_4Ph)_5Cl_2]^{2+}$ (**AuCu-rod**), and paired them with 9,10-bis(phenylethynyl)anthracene (BPEA) annihilator/emitter to explore the impact of Cu-doping on the triplet sensitization and NIR-UC performance. The triplet state of **AuCu-rod**, with lifetime of 3 μs, exhibited a modest blue shift compared to the **Au-rod**, resulting in the increment in the driving force for triplet energy transfer (TET) to the BPEA acceptor. The TET rate constant was determined to be 5.0×10^7 M^{-1} s^{-1}, which is an order of magnitude higher than the rate constant for the **Au-rod**/BPEA pair. This improvement has led to a remarkable increase in the TET efficiency. Notably, the **AuCu-rod**/BPEA pair facilitated the efficient UC of 805 nm NIR light into 510 nm visible light, realizing a large anti-Stokes shift close to 0.9 eV. The UC internal quantum yield of this combination was determined to be 2.33 ± 0.05%, marking a fivefold enhancement over the **Au-rod** sensitizer (0.49%). Thus, alloying NC sensitizers offers a promising route to enhance UC performance by tuning the triplet state energy and optimizing the compatibility between the sensitizer and annihilator. Additionally, in this series of experiments, the formation of small amounts of BPEA microaggregates was observed. These aggregates did not undergo singlet fission and could retain multiple long-lived triplet excitons. This characteristic facilitated TTA among triplet excitons, resulting in efficient NIR-to-visible UC emission.

Received 6th May 2024,
Accepted 1st July 2024

DOI: 10.1039/d4nr01948b

rsc.li/nanoscale

Introduction

Sunlight stands as a clean and sustainable energy source available for human use, with growing expectations for its further effective utilization. Despite encompassing a broad range of wavelengths of light (photon energies) from ultraviolet to infrared, the majority of current solar-driven devices are mainly limited to harnessing light in the ultraviolet and visible regions. Therefore, it is crucial to tap into the range of wavelengths that have remained underutilized thus far. For instance, enhancing the efficiency of utilizing light in the near-infrared (NIR) region is a significant challenge in applications such as photocatalytic hydrogen production[1] and various types of solar cells.[2,3]

Photon upconversion (UC), a method that converts low-energy photons into higher-energy photons, stands out as a promising technique for light-energy conversion. Particularly, triplet–triplet annihilation (TTA)-based upconversion (TTA-UC) is of significant interest as a mechanism that holds promise in addressing the challenge mentioned, because it operates effectively even under standard solar irradiance.[4–8] TTA-UC usually consists of an appropriate combination of a sensitizer and an annihilator (emitter). As illustrated in Scheme 1, in the TTA-UC mechanism, the photoexcited sensitizer in the S_1 state undergoes intersystem crossing (ISC) to produce the triplet (T_1) state. Subsequently, triplet energy transfer (TET) from this triplet sensitizer to a ground-state annihilator occurs. Two of the triplet annihilators thus generated undergo TTA, one transitions to the S_1 state, emitting upconverted fluorescence. Therefore, TTA-UC is a two-photon process, and the maximum

Department of Chemistry, College of Science, Rikkyo University, 3-34-1, Nishiikebukuro, Toshima-ku, Tokyo 171-8501, Japan. E-mail: mitsui@rikkyo.ac.jp

† Electronic supplementary information (ESI) available. See DOI: https://doi.org/10.1039/d4nr01948b

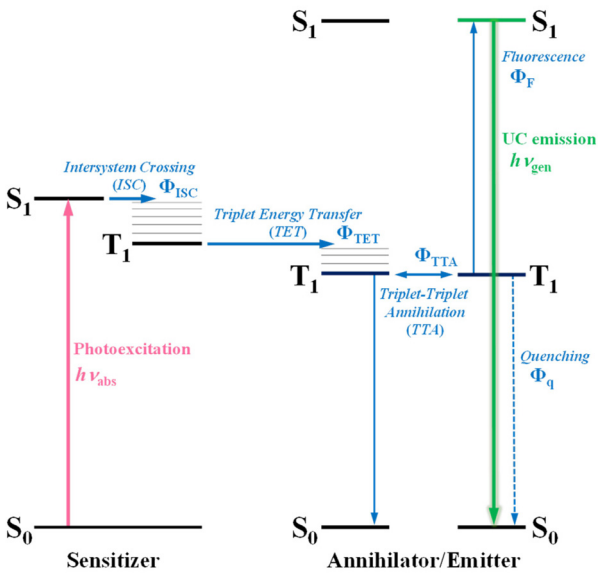

Scheme 1 A Jablonski diagram illustrating the photophysical processes associated with photon upconversion (UC) *via* triplet–triplet annihilation (TTA), utilizing a sensitizer–annihilator/emitter pair.

UC quantum yield is 50%. Importantly, UC quantum yields that remain uncorrected for reabsorption effects pose obstacles when comparing various sensitizer–annihilator pairs due to their significant dependence on sample concentration and the optical path length of the solution. Hence, to ensure consistency in evaluating UC performance, this paper employs the internal UC quantum yield (Φ_{UCg}), defined as the ratio of upconverted photons generated ($\#h\nu_{gen}$) to photons absorbed by the sensitizer ($\#h\nu_{abs}$).[9] The formula for Φ_{UCg} is expressed as follows:

$$\Phi_{UCg} = \frac{\#h\nu_{gen}}{\#h\nu_{abs}} = \frac{1}{2}\Phi_{ISC}\Phi_{TET}\Phi_{TTA}\Phi_{F}(1-\Phi_{q}), \quad (1)$$

where Φ_{ISC} is the ISC quantum yield of the sensitizer, Φ_{TET} is the quantum yield of TET from sensitizer to annihilator, Φ_{TTA} and Φ_F are the formation yield of annihilator in the S_1 state *via* TTA and the fluorescence quantum yield of the annihilator, respectively. Although typically ignored in the general definition of UC quantum yield, Φ_q denotes the quantum yield at which triplet annihilators are quenched by others, such as ground-state sensitisers and molecular oxygen. To approach the maximum value (50%) of Φ_{UCg}, the improvements are required in Φ_{ISC}, Φ_{TET}, Φ_{TTA}, and Φ_F, while Φ_q must approach zero.

Numerous sensitizer–annihilator pairs with Φ_{UCg} exceeding several tens of percent have been reported for visible-to-visible UC in degassed solutions. However, the UC quantum yield from NIR (>700 nm) to visible light remains less than 10%, even at the current highest value,[10] and in most reported systems, a few percent or less.[11] Organometallic complexes with extended π-conjugated frameworks and semiconductor nanocrystals modified with triplet-mediator ligands have been reported as sensitizers for NIR-UC. However, the former generally involves a cumbersome multi-step synthesis,[12–14] while the latter, although easy to synthesize, is restricted to compositions containing highly toxic Pb and Se atoms.[15–18] The choice of sensitizers with strong NIR light absorption and high Φ_{ISC} is indeed considerably limited. Therefore, one of the reasons for the low Φ_{UCg} of NIR-UC is the difficulty in optimizing the combination of sensitizer and annihilator to achieve a high Φ_{TET}.

In recent years, ligand-protected noble-metal nanoclusters (NCs), which allow atomically precise photophysical property tuning, have emerged as powerful triplet sensitizers in TTA-UC.[19–25] Many of the NCs exhibit luminescent lowest excited triplet states generated with nearly 100% efficiency (Φ_{ISC} ~1) and relatively long lifetimes (τ_T) in the range of several microseconds. More noteworthy is that numerous NCs, distinguished by absorption bands extending into the NIR region (>700 nm),[26–28] have been discovered thus far, showcasing their potential as NIR-absorbing sensitizers for TTA-UC. Among them, the superatomic molecular NC depicted in Scheme 2, $[Au_{25}(PPh_3)_{10}(S\text{-}C_2H_4Ph)_5Cl_2]^{2+}$ (hereafter referred to as **Au-rod**), is one such candidate.[29] In **Au-rod**, the long absorption tail originating from the direct S–T transition extends to around 900 nm, and in fact, delayed fluorescence of rubrene based on the TTA-UC mechanism was observed at 785 nm exci-

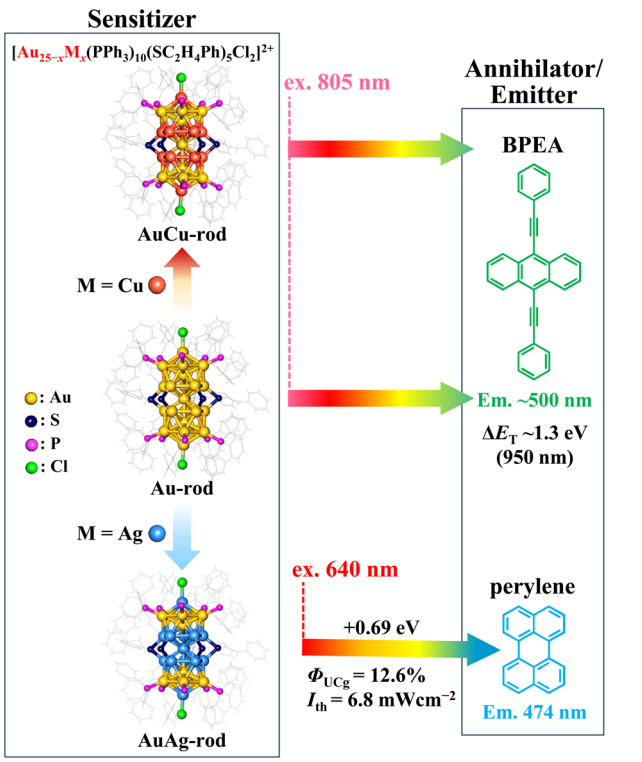

Scheme 2 $[Au_{25}(PPh_3)_{10}(S\text{-}C_2H_4Ph)_5Cl_2]^{2+}$ (**Au-rod**) and its alloy nanoclusters, $[Au_{25-x}Cu_x(PPh_3)_{10}(S\text{-}C_2H_4Ph)_5Cl_2]^{2+}$ (**AuCu-rod**) and $[Au_{25-x}Ag_x(PPh_3)_{10}(S\text{-}C_2H_4Ph)_5Cl_2]^{2+}$ (**AuAg-rod**), were paired with the annihilator/emitter agents BPEA (for NIR-to-visible UC) and perylene (for red-to-blue UC), respectively. Chemical structures of these nanoclusters taken from ref. 30 and 31. The UC performance of **AuAg-rod**, taken from ref. 22, was also presented.

tation.[21] Notably, **Au-rod** possesses the capability to incorporate heteroatoms, such as Ag and Cu, into the bi-icosahedral core.[30,31] Introducing Ag atoms into the bi-icosahedral core of **Au-rod** was found to induce a hypsochromic shift in the absorption band.[22] Our recent study has revealed that this shift is due to the replacement of the central atom of the bi-icosahedral core with an Ag atom, which induces a pronounced higher energy shift of the T_1 state.[22] As a result, the Ag-doped NCs, *i.e.*, $[Au_{25-x}Ag_x(PPh_3)_{10}(S\text{-}C_2H_4Ph)_5Cl_2]^{2+}$ (**AuAg-rod**), served as a sensitizer for red-to-blue UC. In contrast, in the Cu-doped NCs, $[Au_{25-x}Cu_x(PPh_3)_{10}(S\text{-}C_2H_4Ph)_5Cl_2]^{2+}$ (**AuCu-rod**), the absorption bands remain in the NIR region, because the central atom is presumably not replaced by a Cu atom.[31] Therefore, **AuCu-rod**, which does not exhibit the pronounced energy shift in the T_1 state as when Ag-doped, may be a promising sensitizer for NIR-UC. In this study, we initially elucidated the fundamental properties of **AuCu-rod** as a triplet sensitizer. Subsequently, we combined it with the 9,10-bis(phenylethynyl)anthracene (BPEA) annihilator, a green emitter with the T_1 state in the NIR region (E_T ~1.3 eV),[32–35] an extremely low Φ_{ISC} (10^{-5}–10^{-4}),[36] and almost 100% fluorescence quantum yields (Φ_F ~1) independent of the solvent,[37] to assess the performance of NIR-UC. Moreover, it was compared with that of the **Au-rod**/BPEA pair to unravel the impact of Cu doping on the NIR sensitization properties.

Results and discussion

Absorption and emission properties

Fig. 1a shows the absorption spectra of the prepared **AuCu-rod** (average number of Cu-doping: x_{ave} = 5.6, see Fig. S1†). The overall feature of the absorption spectrum, including the first absorption band at 650–800 nm and the absorption peak near 415 nm, were in good agreement with those in the literature.[31] Compared to the absorption tail (730–900 nm) of **Au-rod** (Fig. 1b), the absorption edge of **AuCu-rod** was observed at the shorter wavelength region. Considering that the absorption tail of **Au-rod** is a direct S–T transition from the ground state,[21] the T_1 state of **AuCu-rod** is considered to be somewhat shifted toward shorter wavelength (or higher energy) side. As mentioned earlier, the degree of this blueshift is significantly smaller compared to the case of **AuAg-rod** (x_{ave} = 12), where the shared vertex Au atom in the bi-icosahedron is replaced with the 13th Ag atom.[30] This suggests that in **AuCu-rod**, the shared Au atom is not replaced by the Cu atom, which corresponds with the low average number of doped atoms (x_{ave} = 5.6). According to the literature,[31] the two pentagonal layers (10-atom sites) bonded to the central Au atom in the bi-icosahedral core and the top-site Au atoms coordinated by Cl atoms (2-atom sites) are preferentially replaced by Cu atoms (Scheme 2). The number of introduced Cu atoms (x) in the alloy NCs synthesized ranged from 1 to 10, suggesting the coexistence of alloy NCs in which some of the 12-atom sites are partially replaced by Cu atoms. The molar absorption coefficient (ε) at 805 nm was determined to be 470 M^{-1} cm^{-1}, decreasing to nearly zero at around 840 nm. Similar to **Au-rod**, this absorption edge region of **AuCu-rod** should originate from S–T transitions, so that the T_1 state of **AuCu-rod** presumably resides around 1.5 eV. Therefore, an exothermic TET process from the **AuCu-rod** sensitizer to the BPEA annihilator (E_T ~1.3 eV) is expected.

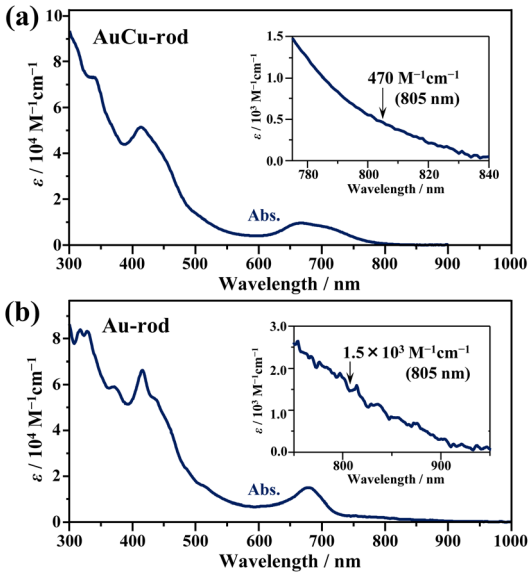

Fig. 1 Absorption spectra of (a) **AuCu-rod** and (b) **Au-rod** in tetrahydrofuran. The insets display expanded views of the absorption edge region, together with the molar absorption coefficients of the nanoclusters at the excitation light of 805 nm used in the upconversion measurements.

As depicted in Fig. 2a, **AuCu-rod** displays a NIR emission spectrum with a peak at around 810 nm. The excitation spectrum, obtained by monitoring this emission, aligned consistently with the absorption spectrum, confirming the origin of the observed emission from **AuCu-rod**. This emission remains unaffected by oxygen, with no discernible change in intensity or lifetime (3.1 μs) observed under air-saturated conditions. The time evolution of transient absorption (TA) spectra presented in Fig. 2b revealed a ground-state breach (GSB) at wavelengths below 469 nm and broad excited-state absorption (ESA) band at longer wavelengths (>469 nm). Both bands were observed within 0.1 ns immediately after the 670 nm excitation, with decay times of 2–3 μs. The agreement between the ESA decay time constants and the emission lifetime indicates an identical excited state kinetics are probed in both spectroscopic measurements.

Triplet nature and triplet sensitization

To gain insight into the triplet nature of this excited state, quenching experiments were performed using BPEA as an acceptor, and the results are depicted in Fig. 3. As evident from Fig. 3a and b, the addition of BPEA (5 mM) shortened the decay time of the ESA band to 1.9 μs. Additionally, a new band emerged below 500 nm, with a prolonged decay time (154 μs), indicative of the triplet–triplet (T–T) absorption of BPEA.[38] This observation provides clear evidence for TET from

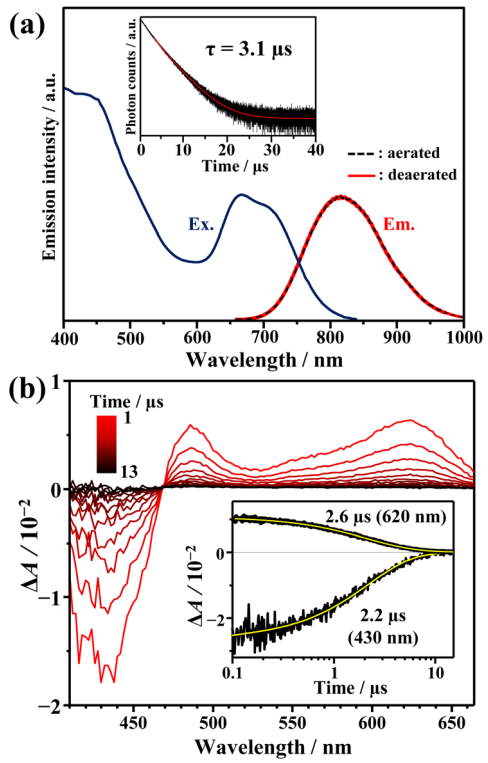

Fig. 2 (a) Excitation (monitored at 850 nm) and emission spectra of **AuCu-rod** (10 μM) in THF. The inset shows the emission decay curve of **AuCu-rod** in deaerated THF. (b) Time evolution of transient absorption (TA) spectra, measured for **AuCu-rod** (47 μM) in deaerated THF (pump at 670 nm). The inset shows the corresponding kinetic traces of the TA signal at 430 and 620 nm.

AuCu-rod to BPEA and establishes that the observed NIR emission is phosphorescence. In line with the behavior observed in **Au-rod** and **AgAu-rod**,[21,22] **AuCu-rod** exhibited no fluorescence signal, coupled with the rapid triplet formation. Thus, it can be inferred that the Φ_{ISC} is nearly unity in the case of **AuCu-rod** as well. Note that the lack of phosphorescence quenching by oxygen can be attributed to the positive Gibbs free energy change (ΔG_{CT} = +0.39 eV, Table S1†) in the oxygen quenching process that proceeds *via* the charge transfer mechanism.[23]

Interestingly, concurrent with the decay of the T–T absorption of BPEA, a weak GSB signal was observed gradually rising around 540–560 nm (Fig. 3c). Furthermore, this GSB signal exhibited a considerably slow decay over a lifetime of nearly 1 ms. This GSB band closely corresponds to the absorption band around 550 nm observed for high concentrations of BPEA (upper part of Fig. 3d) and is therefore considered to originate from small amounts of BPEA aggregates formed in the THF solution. Dynamic light scattering (DLS) measurements for a 20 mM BPEA/THF solution confirmed the formation of BPEA aggregates, with sizes ranging from 0.6 μm to 1 μm (Fig. S2†). The absorption peak of the aggregates (547 nm) is situated on the longer wavelength side compared to lowest-energy absorption peak (498 nm) of the reported nanoparticles with an average diameter of 170 nm.[39] In addition, the aggregates exhibited emission spectra with peaks at 561 nm and 604 nm (bottom part of Fig. 3d). Note that the peak around 520 nm originates from the fluorescence of the BPEA monomer. However, the peak

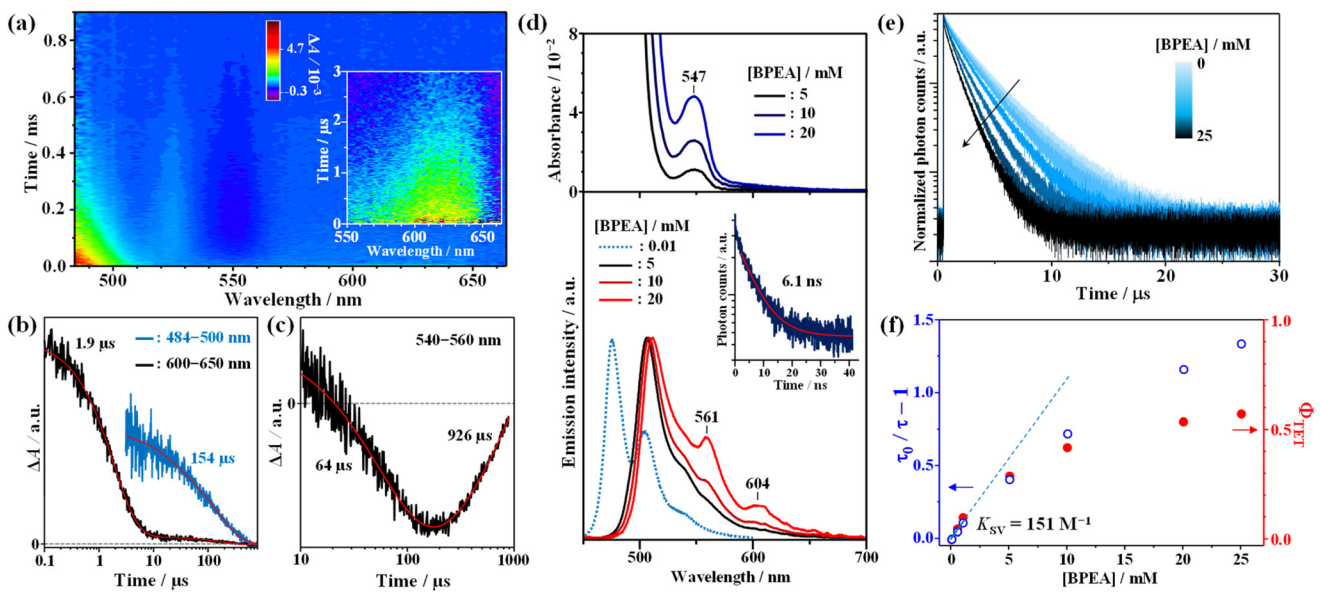

Fig. 3 (a) Two-dimensional time-resolved transient absorption (TA) color maps alongside TA kinetic time traces at specific wavelength intervals: (b) 484–500 nm and 600–650 nm, and (c) 540–560 nm. These were obtained for **AuCu-rod** (47 μM)/BPEA (5 mM) in deaerated tetrahydrofuran (THF), employing a pump wavelength of 670 nm. (d) The relationship between concentration and the spectral properties, namely absorption (top) and emission (bottom), for BPEA is delineated. Additionally, the fluorescence spectrum of a dilute BPEA solution (10 μM) is depicted (dotted line) in the lower panel for comparison. (e) BPEA concentration dependence of the emission decay curves for **AuCu-rod** (20 μM) in deaerated THF are displayed as a function of the (0–20 mM), following excitation at 634 nm. (f) Stern–Volmer plot based on the emission lifetimes and the BPEA-concentration dependence of triplet energy transfer quantum yield (Φ_{TET}).

wavelength is an apparent value caused by reabsorption by BPEA. It is noteworthy that the spectral feature of this emission closely resembles that of the one-dimensional microrods of BPEA.[40] The emission lifetime obtained by monitoring emission signals above 560 nm is 6.1 ns, which is longer than the lifetime of the monomer emission (3.2 ns), and distinctly different from the nanoparticles with a very short emission lifetime (20 ps) due to non-radiative deactivation *via* singlet fission (SF).[39] Hence, the formed BPEA aggregates possess an electronic structure and packing morphology in which SF is less likely to occur. Notably, the very slow rise (64 μs) and decay GSB (926 μs) signals indicate that the slow TET from triplet BPEA monomers to aggregates occurs, with the triplet energy being retained as triplet excitons in the aggregate for an extended period. This phenomenon has significant implications for the TTA-UC performance, as discussed below.

As depicted in Fig. 3e, a decrease in phosphorescence lifetime was observed with increasing BPEA concentration. To determine the TET rate constant (k_{TET}), a Stern–Volmer analysis was conducted on the BPEA concentration dependence of the phosphorescence lifetime. As shown in Fig. 3f, the Stern–Volmer plot exhibited a linear relationship for BPEA concentrations below 1 mM, transitioning to a gradually saturating behavior in the high concentration region (≥5 mM). This nonlinear response with respect to BPEA concentration is reminiscent of the behavior observed in the **Au-rod**/BPEA system[21] and can be attributed to the formation of BPEA aggregates in the high concentration region (Fig. 3d and Fig. S2†). Through fitting the linearly dependent region free from aggregation effects, the k_{TET} value were determined to be and 5.0×10^7 M^{-1} s^{-1} (Stern–Volmer constant (K_{SV}) of 151 M^{-1}). This value is 10-fold larger than that of **Au-rod** (4.6×10^6 M^{-1} s^{-1}).[21] Since the surface ligand environments of **AuCu-rod** and **Au-rod** are identical, this improvement is a result of a blue shift of the T_1 state due to Cu doping, which increases the driving force of the TET process to the BPEA acceptor. When tetracene (E_T = 1.27 eV) and rubrene (1.14 eV), which possess similar or lower T_1 energies compared to BPEA (~1.3 eV), were utilized as acceptors to evaluate k_{TET}, they yielded k_{TET} of 6.3×10^7 M^{-1} s^{-1} and 5.9×10^7 M^{-1} s^{-1}, respectively (Fig. S3 and Table S2†). These rate constants were of similar magnitude to that of BPEA. Conversely, when perylene (E_T = 1.53 eV), which has a higher T_1 energy than BPEA, was employed as an acceptor, the k_{TET} decreased to 1.5×10^7 M^{-1} s^{-1}. From these results, it can be inferred that the T_1 state of **AuCu-rod** is indeed located around 1.5 eV, which also corresponds well with the fact that the absorption band edge based on the direct S–T transition from the ground state was observed at around 830 nm (see Fig. 1a). The maximum value of k_{TET} (7.1×10^7 M^{-1} s^{-1}) of **AuCu-rod** is one order of magnitude smaller than that of NCs with electronic states (hole and electron distributions) extending to the surface ligands.[24,25] This large difference can be attributed to the fact that the T_1 state of **AuCu-rod** is mainly localized on the metal core, with the hole and electron distribution being sterically shielded from the external environment by the surface ligands (PPh_3 and S-C_2H_4Ph). The Φ_{TET} values was obtained using the following equation:

$$\Phi_{TET} = 1 - \frac{\tau}{\tau_0}, \quad (2)$$

where τ_0 is the phosphorescence lifetime of the sensitizer (τ_0 = 3.1 μs for **AuCu-rod** and τ_0 = 3.4 μs for **Au-rod**) and τ is the lifetime of the sensitizer when BPEA is added. At a BPEA concentration of 20 mM, the Φ_{TET} of **AuCu-rod** was calculated to be 54% (τ = 1.5 μs), while that of **Au-rod** is 18% (τ = 2.8 μs) as per eqn (2). This represents a threefold improvement in Φ_{TET} attributable to alloying.

Near-infrared photon upconversion performance

Fig. 4a depicts the emission spectrum obtained from a deaerated THF solution containing **AuCu-rod** (50 μM) and BPEA (20 mM) obtained when excited with a the continuous-wave 805(±2)-nm laser. Strong UC emission with peaks at 507, 561, and 604 nm was observed at wavelengths shorter than the excitation light. As evident from the comparison with Fig. 3d and the UC emission spectrum measured before BPEA reached dissolution equilibrium, the emission around 507 nm is primarily attributed to fluorescence from BPEA monomers. Meanwhile,

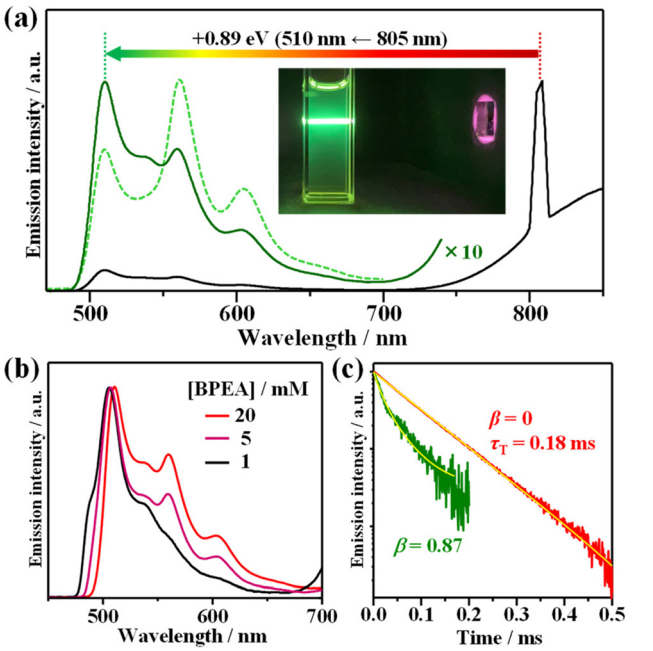

Fig. 4 (a) Upconversion (UC) emission spectra of a mixture containing **AuAc-rod** (50 μM) and BPEA (20 mM) in deaerated THF, observed under continuous wave 805 nm laser excitation (5.1 W cm^{-2}), and a photographic image of the UC emission captured without any filters. The dashed line represents the UC spectrum of the mixture measured before BPEA reached dissolution equilibrium. (b) UC spectra of mixtures containing **AuAc-rod** (50 μM) and BPEA at concentrations of 1, 5, and 20 mM. (c) UC emission decay curves obtained using appropriate filters for either monomer UC emission ($\lambda \leq$ 525 nm, solid green line) or aggregate UC emission ($\lambda \geq$ 625 nm, solid red line). The yellow solid lines represent least-square fitting curves obtained using eqn (3).

the longer wavelength portion featuring peaks at 561 nm and 604 nm originates from the emission from BPEA aggregates. This is also clear from the influence of BPEA concentration on the UC spectra. As shown in Fig. 4b, as the BPEA concentration increased, the contribution of UC emission from the aggregates (peaks at 561 and 604 nm) progressively increased.

Fig. 4c shows the decay profiles of each UC emission, observed using appropriate filters to separate the emissions. In a semi-logarithmic plot, the monomer UC emission decay exhibited a pronounced concave curvature, whereas the UC emission decay derived from aggregates was almost linear. These differences in behaviour reflect the varying degrees of TTA influence on the deactivation processes of triplet BPEA monomers and triplet excitons in aggregates. The time trace of UC emission intensity, $I_{UC}(t)$, can be analysed using the following equation:[41]

$$I_{UC}(t) \propto \left[{}^3\mathrm{BPEA}^*\right]_t^2 = \left[{}^3\mathrm{BPEA}^*\right]_0^2 \left(\frac{1-\beta}{\exp\left(\frac{t}{\tau_T}\right)-\beta}\right)^2, \quad (3)$$

where $\left[{}^3\mathrm{BPEA}^*\right]_0$ is the triplet concentration of BPEA at time zero (t = 0), $\left[{}^3\mathrm{BPEA}^*\right]_t$ is the triplet concentration of BPEA at time t, τ_T is the triplet lifetime of BPEA, and the dimensionless parameter β corresponds to the relative contribution of initial triplet deactivation by TTA, as eqn (4).

$$\beta = \frac{2k_{TTA}\left[{}^3\mathrm{BPEA}^*\right]_0}{\tau_T^{-1} + 2k_{TTA}\left[{}^3\mathrm{BPEA}^*\right]_0} \ (0 < \beta < 1), \quad (4)$$

where k_{TTA} is the second-order rate constant of the TTA process. Fitting the monomer UC decay yielded a β value of 0.87 (τ_T = 0.34 ms), indicating that TTA dominates the deactivation pathway of the triplet BPEA monomers. Note that the parameter τ_T can be most accurately determined when the value of β is close to 0.5, while the precision of τ_T values obtained when β approaches 1 is significantly reduced.[42] Therefore, the τ_T value obtained for monomer UC decay is considerably less precise. Contrastingly, the decay of UC emission in BPEA aggregates was best described by a single exponential function (*i.e.*, β = 0, τ_T = 0.18 ms), indicating that triplet decay *via* TTA is inefficient in the aggregates. This is considered to arise from the small amounts of triplet excitons generated within the aggregates through slow TET from triplet monomers. This may reflect the very low concentration of the aggregates formed, denoted as [Agg]. For instance, at a BPEA concentration of 5 mM, the rise of the GSB signal from the aggregates is quite slow (see Fig. 3c), with a rise time of 64 μs (*i.e.*, $k_{TET(Agg)}$[Agg] = 1.6×10^4 s^{-1}, where $k_{TET(Agg)}$ represents the TET rate constant from BPEA monomers to BPEA aggregates). Assuming a diffusion-limited rate constant of ~10^{10} M^{-1} s^{-1} for $k_{TET(Agg)}$, the concentration of aggregates is estimated to be ~1 μM. Despite such a low concentration, the BPEA aggregates exhibit relatively strong UC emission (Fig. 4b), suggesting efficient TTA among triplet excitons within the aggregates.

Fig. 5a shows the excitation intensity-dependent Φ_{UCg} (out of 50% maximum) of **AuCu-rod** (50 μM) or **Au-rod** (50 μM) with

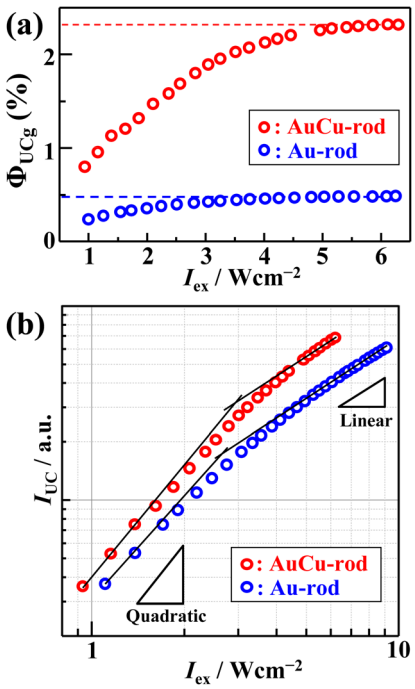

Fig. 5 Excitation intensity (I_{ex}) dependence of (a) upconversion (UC) internal quantum yield (Φ_{UCg}) and (b) UC emission intensity (I_{UC}). For comparison, results from a mixture of 50 μM **AuCu-rod** and 20 mM BPEA are also shown.

BPEA (20 mM), obtained using the relative method (eqn (S1)†). From the saturation region of Φ_{UCg} beyond 5 W cm^{-2}, the maximum values of Φ_{UCg} were determined to be 2.33 ± 0.05% for **AuCu-rod** and 0.49 ± 0.01% for **Au-rod** (Fig. S4 and S5†). Thus, an improvement in Φ_{UCg} by 4.7-fold was observed, which mainly reflects the 3-fold enhancement in Φ_{TET}. As a comparison, Table 1 presents the literature values of Φ_{UCg} when excited near 800 nm for solution systems employing various sensitizers. The Φ_{UCg} of **AuCu-rod** is significantly superior to those of PbSe and PbS nanoparticles without transmitter ligands, but inferior to those of the nanoparticles with

Table 1 Internal UC quantum yield (Φ_{UCg}) for a deaerated tetrahydrofuran (THF) solution of **AuCu-rod** (50 μM) or **Au-rod** (50 μM) sensitizer mixed with BPEA annihilator (20 mM). For comparison, literature values of Φ_{UCg} obtained with excitation near 800 nm in solution systems containing other sensitizers are also provided[a]

Sensitizer	Annihilator	λ_{ex}/nm	Φ_{UCg} (%)
AuCu-rod	BPEA	805	2.33 ± 0.05
Au-rod	BPEA	805	0.49 ± 0.01
PbSe[b]	Rubrene	800	0.1
PbSe/CPT[b]	Rubrene	808	1.05
PbS[b]	Rubrene	808	0.0105
PbS/CPT[b]	Rubrene	808	0.85
PbS/CdS/5-CAT[c]	Rubrene	808	4.2
PbS/Th-DPP[d]	Rubrene	808	6.8

[a] Values reported with a maximum of 100% were halved. [b] Ref. 16. [c] Ref. 43. [d] Ref. 44.

transmitter ligands. As mentioned earlier, the Φ_{TET} of **AuCu-rod** is 0.54 at 20 mM BPEA, suggesting there is considerable potential for enhancement. Recent findings from our group indicate that the TET rate constant can be markedly improved by incorporating triplet-mediator ligands that maintain the triplet energy, even in ligand-protected metal nanoclusters.[45] Therefore, applying this approach to **Au-rod** and **AuCu-rod** is anticipated to further enhance the NIR-UC efficiency. The development of such systems is currently in progress within our group.

The dependence of UC emission intensity (I_{UC}) on excitation intensity (I_{ex}), as depicted in Fig. 5b, exhibits a shift from quadratic to linear behavior in the UC emission intensity. This transition marks the determination of the UC threshold intensity (I_{th}), a critical performance metric for the TTA-UC system, which was identified at 2.9 W cm^{-2}. Note that an almost identical magnitude of I_{th} = 2.5 W cm^{-2} was obtained for **Au-rod** (Fig. 5b). I_{ex} is expressed by the following:[46]

$$I_{th} \propto \frac{1}{(1-10^{-A(\lambda_{ex})})\Phi_{ISC}\Phi_{TET}k_{TTA}\tau_{T(A)}{}^2}, \quad (5)$$

where $A(\lambda_{ex})$ is the absorbance at the excitation wavelength (λ_{ex}) of the sensitizer and $\tau_{T(A)}$ is the triplet lifetime of the annihilator. According to this equation, one of the primary factors contributing to the high I_{th} could be the low light-harvesting efficiency, *i.e.*, $(1–10^{-A(\lambda_{ex})})$, for **AuCu-rod** under UC measurement conditions (λ_{ex} = 805 nm), which was only 5.2%. This low efficiency is attributed to the small ε (805) of **AuCu-rod**, which is 470 M^{-1} cm^{-1} (Fig. 1a). In contrast, while the ε (805) value of **Au-rod** is approximately three times higher (Fig. 1b), the Φ_{TET} of **Au-rod** is 1/3 of that of **AuCu-rod**. This compensatory effect led to a similar I_{th} being obtained for both sensitizers.

Fig. 6 illustrates a proposed energy-level diagram for the photophysical processes occurring in a TTA-UC system comprising the **AuCu-rod** sensitizer and BPEA annihilator. The excitation of **AuCu-rod** at 805 nm is anticipated to directly induce the electronic transition from the ground state to the triplet state. Such direct generation of the sensitizer triplets offers the advantage of suppressing energy loss during the ISC process and increasing the anti-Stokes shift. Indeed, the system successfully converted 805 nm NIR light into 510 nm visible light, achieving an anti-Stokes shift approximately 300 nm in wavelength and 0.9 eV in energy. TET from the triplet **AuCu-rod** sensitizer to BPEA monomers, followed by TTA among the triplet monomers, results in green UC emission. In addition, some triplet monomers occur TET to BPEA aggregates, generating multiple triplet excitons in the aggregates. As a result, TTA occurs within the aggregates, leading to yellow UC emission from the aggregates that is shifted to longer wavelengths compared to the monomer UC emission. The S_1 state energy (E_S) of the aggregates was estimated to be around 2.23 eV (555 nm) based on the intersection of their absorption and emission spectra (Fig. 3d). This is a shift from the S_1 energy of the monomer (2.64 eV) to an energy approximately 0.4 eV lower, which reflects the singlet exciton coupling strength of the aggregates.

As can be seen in Fig. 4b, the impact of BPEA concentration on the UC spectrum reveals a significant escalation in the contribution of UC emission from aggregates as the BPEA concentration rises. Despite this augmentation, the UC quantum yield (Φ_{UCg}) maintains a nearly linear growth (Fig. S6†). Considering that beyond 10 mM concentration, the increment in Φ_{TET} diminishes and nears saturation (refer to Fig. 3f), the linear enhancement of Φ_{UCg} with higher BPEA concentrations could be attributed to the superior Φ_{TTA} within the aggregates, offsetting the reduced gains in Φ_{TET}. In the case of BPEA monomers, the energy of the S_1 state (E_S) is approximately twice that of the T_1 state, with the $E_S - 2E_T$ difference being only 30 meV.[35] However, within aggregates, the stronger singlet exciton coupling compared to that of triplet excitons,[35] the relative energy relationship may change to $E_S < 2E_T$. This variation not only promotes TTA but also inhibits SF, which is consistent with the experimental observations. Another contributing factor might be the anisotropic growth of aggregates into one-dimensional (1D) microrods aligned along the π–π stacking direction,[40] which would primarily limit exciton migration to this 1D pathway. Such spatial restriction is likely to heighten the encounter rate among triplet excitons,[47] thereby elevating Φ_{TTA}. Hence, the current results suggest the usefulness of low-dimensional BPEA aggregates as a platform for efficient TTA in NIR-UC applications, warranting further investigation.

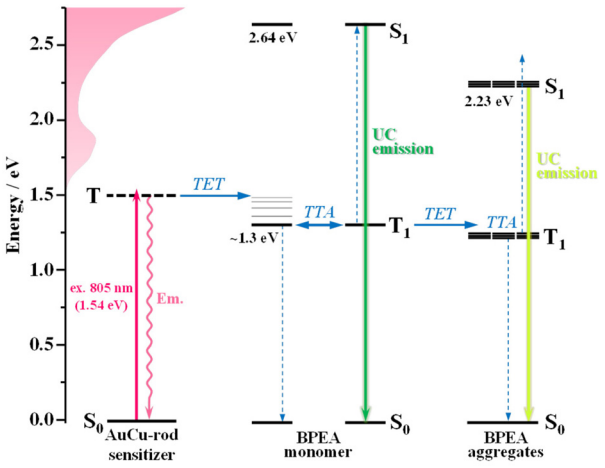

Fig. 6 Schematic energy level diagram of the TTA-UC process in a system comprising the **Au-rod** sensitizer and 9,10-bis(phenylethynyl) anthracene (BPEA) annihilator monomer and aggregates. TET = triplet energy transfer and TTA = triplet–triplet annihilation.

Conclusions

In summary, we explored the photophysical characteristics and NIR-UC performance of **AuCu-rod** acting as a triplet sensitizer, in combination with a BPEA annihilator, and compared the results with those from an **Au-rod**/BPEA sensitizer-annihilator pair. Our findings revealed that Cu-substitution leads to a

moderate blue shift in the triplet state, markedly improving both TET and UC quantum yields relative to the **Au-rod**/BPEA combination. Interestingly, we also discovered that micro-aggregates of BPEA annihilators serve as a highly effective platform for TTA and subsequent UC emission. The findings underscore the significance of fine-tuning the triplet state energy *via* atomic-level alloying of the NIR-absorbing NC sensitizers to refine the synergy between sensitizer and annihilator, thereby enhancing TET efficiency and NIR-UC performance. Considering the abundance of ligand-protected noble-metal NCs capable of absorbing NIR light, the pursuit of these promising strategies is anticipated to further improve the performance of NIR-UC in the future.

Author contributions

Yuki Miyoshi: experiment, data acquisition, analysis. Daichi Arima: experiment, data acquisition, analysis. Masaaki Mitsui: supervision, writing – revision and editing, theoretical calculations, and funding acquisition.

Data availability

The data supporting this article have been included as part of the ESI.†

Conflicts of interest

There are no conflicts to declare.

Acknowledgements

This work is partly supported by the Grant-in-Aids for Scientific Research (C), no. 20K05653 and Scientific Research (B), no. 24K01614 and the 45th Japan Sheet Glass Society for the Promotion of Materials Science and Engineering Research Grant. The authors thank Dr Shusaku Nagano of Rikkyo University for the loan of the dynamic light scattering equipment.

References

1 Q. Wang and K. Domen, *Chem. Rev.*, 2020, **120**, 919–985.
2 J. M. Cole, G. Pepe, O. K. A. Bahri and C. B. Cooper, *Chem. Rev.*, 2019, **119**, 7279–7327.
3 G. Zhang, F. R. Lin, F. Qi, T. Heumüller, A. Distler, H.-J. Egelhaaf, N. Li, P. C. Y. Chow, C. J. Brabec, A. K.-Y. Jen and H.-L. Yip, *Chem. Rev.*, 2022, **122**, 14180–14274.
4 D. V. Kozlov and F. N. Castellano, *Chem. Commun.*, 2004, 2860.
5 S. Baluschev, T. Miteva, V. Yakutkin, G. Nelles, A. Yasuda and G. Wegner, *Phys. Rev. Lett.*, 2006, **97**, 143903.
6 A. Monguzzi, J. Mezyk, F. Scotognella, R. Tubino and F. Meinar, *Phys. Rev. B: Condens. Matter Mater. Phys.*, 2008, **78**(19), 5112.
7 Y. Y. Cheng, T. Khoury, R. G. C. R. Clady, M. J. Y. Tayebjee, N. J. Ekins-Daukes, M. J. Crossley and T. W. Schmidt, *Phys. Chem. Chem. Phys.*, 2010, **12**, 66–71.
8 T. N. Singh-Rachford and F. N. Castellano, *Coord. Chem. Rev.*, 2010, **254**, 2560–2573.
9 Y. Zhou, F. N. Castellano, T. W. Schmidt and K. Hanson, *ACS Energy Lett.*, 2020, **5**, 2322–2326.
10 W. Liang, C. Nie, J. Du, Y. Han, G. Zhao, F. Yang, G. Liang and K. Wu, *Nat. Photonics*, 2023, **17**, 1–8.
11 P. Bharmoria, H. Bildirir and K. Moth-Poulsen, *Chem. Soc. Rev.*, 2020, **49**, 6529–6554.
12 V. Yakutkin, S. Aleshchenkov, S. Chernov, T. Miteva, G. Nelles, A. Cheprakov and S. Baluschev, *Chem. – Eur. J.*, 2008, **14**, 9846–9850.
13 T. N. Singh-Rachford, A. Nayak, M. L. Muro-Small, S. Goeb, M. J. Therien and F. N. Castellano, *J. Am. Chem. Soc.*, 2010, **132**, 14203–14211.
14 S. Amemori, N. Yanai and N. Kimizuka, *Phys. Chem. Chem. Phys.*, 2015, **17**, 22557–22560.
15 Z. Huang, X. Li, M. Mahboub, K. M. Hanson, V. M. Nichols, H. Le, M. L. Tang and C. J. Bardeen, *Nano Lett.*, 2015, **15**, 5552–5557.
16 Z. Huang, D. E. Simpson, M. Mahboub, X. Li and M. L. Tang, *Chem. Sci.*, 2016, **7**, 4101–4104.
17 Z. Huang, X. Zihao, M. Mahboub, Z. Liang, P. Jaimes, P. Xia, K. R. Graham, M. L. Tang and T. Lian, *J. Am. Chem. Soc.*, 2019, **141**(25), 9769–9772.
18 N. Nishimura, J. R. Allardice, J. Xiao, Q. Gu, V. Gray and A. Rao, *Chem. Sci.*, 2019, **10**, 4750–4760.
19 Y. Niihori, Y. Wada and M. Mitsui, *Angew. Chem., Int. Ed.*, 2021, **60**, 2822–2827.
20 D. Arima, Y. Niihori and M. Mitsui, *J. Mater. Chem. C*, 2022, **10**, 4597–4606.
21 M. Mitsui, Y. Wada, R. Kishii, D. Arima and Y. Niihori, *Nanoscale*, 2022, **14**, 7974–7979.
22 M. Mitsui, D. Arima, Y. Kobayashi, E. Lee and Y. Niihori, *Adv. Opt. Mater.*, 2022, **10**, 2200864.
23 M. Mitsui, D. Arima, A. Uchida, K. Yoshida, Y. Arai, K. Kawasaki and Y. Niihori, *J. Phys. Chem. Lett.*, 2022, **13**, 9272–9278.
24 D. Arima and M. Mitsui, *J. Am. Chem. Soc.*, 2023, **145**, 6994–7004.
25 M. Mitsui and A. Uchida, *Nanoscale*, 2024, **16**, 3053–3060.
26 (*a*) R. Jin, *Nanoscale*, 2015, **7**, 1549–1565; (*b*) X. Kang, Y. Li, M. Zhu and R. Jin, *Chem. Soc. Rev.*, 2020, **49**, 6443–6514.
27 M. S. Bootharaju, V. M. Burlakov, T. M. D. Besong, C. P. Joshi, L. G. AbdulHalim, D. M. Black, R. L. Whetten, A. Goriely and O. M. Bakr, *Chem. Mater.*, 2015, **27**, 4289–4297.
28 X. Kang, H. Chong and M. Zhu, *Nanoscale*, 2018, **10**, 10758–10834.
29 (*a*) Y. Shichibu, Y. Negishi, T. Watanabe, N. K. Chaki, H. Kawaguchi and T. Tsukuda, *J. Phys. Chem. C*, 2007, **111**,

7845; (*b*) H. Qian, W. T. Eckenhoff, M. E. Bier, T. Pintauer and R. Jin, *Inorg. Chem.*, 2011, **50**, 10735–10739.
30 S. Wang, X. Meng, A. Das, T. Li, Y. Song, T. Cao, X. Zhu, M. Zhu and R. Jin, *Angew. Chem., Int. Ed.*, 2014, **53**, 2376.
31 S. Yang, J. Chai, T. Chen, B. Rao, Y. Pan, H. Yu and M. Zhu, *Inorg. Chem.*, 2017, **56**, 1771–1774.
32 Y. J. Bae, J. A. Christensen, G. Kang, J. Zhou, R. M. Young, Y.-L. Wu, R. P. Van Duyne, G. C. Schatz and M. R. Wasielewski, *J. Chem. Phys.*, 2019, **151**, 044501.
33 V. Gray, A. Dreos, P. Erhart, B. Albinsson, K. M.-Poulsen and M. Abrahamsson, *Phys. Chem. Chem. Phys.*, 2017, **19**, 10931–10939.
34 F. Zhong and J. Zhao, *Dyes Pigm.*, 2017, **136**, 909–918.
35 S. Jana, A. L. Yapamanu and S. Umapathy, *Phys. Chem. Chem. Phys.*, 2019, **21**, 14341–14349.
36 M. Mitsui, Y. Kawano, R. Takahashi and H. Fukui, *RSC Adv.*, 2012, **2**, 9921–9931.
37 A. Demeter, *J. Phys. Chem. A*, 2014, **118**, 9985–9993.
38 T.-S. Fang, J. Lin, R. Schneider, T. Yamada and L. A. Singer, *Chem. Phys. Lett.*, 1982, **92**, 283–287.
39 B. Manna, A. Nandi and R. Ghosh, *J. Phys. Chem. C*, 2018, **122**, 21047–21055.
40 Y. S. Zhao, J. Xu, A. Peng, H. Fu, Y. Ma, L. Jiang and J. Yao, *Angew. Chem., Int. Ed.*, 2008, **47**, 7301–7305.
41 S. M. Bachilo and R. B. Weisman, *J. Phys. Chem. A*, 2000, **104**, 7711–7714.
42 F. Edhborg, A. Olesund and B. Albinsson, *Photochem. Photobiol. Sci.*, 2022, **21**, 1143–1158.
43 M. Mahboub, Z. Huang and M. L. Tang, *Nano Lett.*, 2016, **16**, 7169–7175.
44 L.-H. Jiang, X. Miao, M.-Y. Zhang, J.-Y. Li, L. Zeng, W. Hu, L. Huang and D.-W. Pang, *J. Am. Chem. Soc.*, 2024, **146**, 10785–10797.
45 D. Arima, S. Hidaka, S. Yokomori, Y. Niihori, Y. Negishi, R. Oyaizu, T. Yoshinami, K. Kobayashi and M. Mitsui, *J. Am. Chem. Soc.*, 2024, **146**, 16630–16638.
46 Y. Murakami and K. Kamada, *Phys. Chem. Chem. Phys.*, 2021, **23**, 18268–18282.
47 R. Sato, H. K.-Nishioka, K. Kamada, T. Mizokuro, K. Kobayashi and Y. Shigeta, *J. Phys. Chem. Lett.*, 2018, **9**, 6638–6643.